Simultaneous flow measurement and deformation tracking for passive flow control experiments involving fluid–structure interactions

Wolf Iring Kösters, Stefan Hoerner

Journal of Fluids and Structures 121 (2023) 103956

Contents lists available at ScienceDirect

Journal of Fluids and Structures

journal homepage: www.elsevier.com/locate/jfs

Simultaneous flow measurement and deformation tracking for passive flow control experiments involving fluid–structure interactions

Wolf Iring Kösters [a,b,*], Stefan Hoerner [a]

[a] Laboratory of Fluid Dynamics and Technical Flows, Institute of Fluid Dynamics and Thermodynamics, Otto von Guericke University Magdeburg (OvGU), Universitaetsplatz 2, 39106 Magdeburg, Germany

[b] Center for Biorobotics, Tallinn University of Technology (Taltech), Akadeemia tee 15A, 12616 Tallinn, Estonia

ARTICLE INFO

Article history:
Received 10 January 2023
Received in revised form 12 July 2023
Accepted 18 July 2023
Available online xxxx

Dataset link: 10.24352/UB.OVGU-2022-085, https://github.com/ikoesters/FSI_tracking

Keywords:
Fluid–structure interaction
Deformation tracking
PIV
Masking
NACA0018 hydrofoil
Passive flow control

ABSTRACT

Fluid–structure interactions (FSI) on highly flexible structures involve large deformations and require specific techniques for a thorough investigation of the flow field and structural deformation. To this purpose, a physics-informed method is introduced that allows for simultaneous determination of the flow fields and the structural deformation by using Particle Image Velocimetry (PIV) raw images. The method combines apriori knowledge of the mechanical characteristics of the flexible structure with classical image processing techniques for segmentation. PIV recordings of an actively pitched, highly deformable hydrodynamic profile experiment in a closed water tunnel serve as an example case. To achieve accurate results, the contour obtained from image segmentation is further defined under the assumption that its flexure can be described with the Euler–Bernoulli beam theory model. This makes it possible to determine the neutral fiber of the structure and the final reconstruction becomes possible from knowledge of the original geometry. The resulting procedure allows for a recognition of the structure itself and is suitable for cross-section deformation measurements and for masking of the structure in the raw images to improve the PIV processing. A test case comprising synthetic data similar to the application with a modeled profile geometry of known shape is used to investigate the accuracy of the method and its validity for deformation measurements. Under conditions of cyclic dynamic stall, a mean absolute error of 0.84° could be reached, with a deterioration up to 2° mean absolute error under static stall. The method has a major advantage compared to other technically more sophisticated and complex methods, such as the combination of Laser interferometers combined with Laser-Doppler Anemometry: the method allows for the usage of a single data source for both, fluid and solid in a unified measurement method. Therefore a direct comparison of instantaneous flow field and deformation is possible. In consequence it is in particular useful for highly dynamic multi-physical processes involving extreme deformations, such as passive flow control and soft actuated or flexible under water robotics.

* Corresponding author at: Laboratory of Fluid Dynamics and Technical Flows, Institute of Fluid Dynamics and Thermodynamics, Otto von Guericke University Magdeburg (OvGU), Universitaetsplatz 2, 39106 Magdeburg, Germany.
E-mail address: wolf.koesters@ovgu.de (W.I. Kösters).

https://doi.org/10.1016/j.jfluidstructs.2023.103956

Nomenclature

2D2C	two directions, two components
C	normalized position on the mean-line (chord-line)
FSI	fluid–structure interaction
IoU	intersection over union
IQR	interquartile range
LEGI	Laboratoire des Ecoulements Geophysiques et Industriels
LIF	laser-induced fluorescence
MRI	magnetic resonance imaging
NACA	National Advisory Committee for Aeronautics
px	pixel within frames to be segmented
RMSE	root-mean-square error

1. Introduction

Flexible underwater structures are commonplace in nature. They are required for the undulatory locomotion of aquatic animals including fish, pinnipeds, and cetaceans. In the context of bio-inspired technologies they can also provide substantial benefits for technical applications including soft actuated and flexible underwater robots (Bozkurttas et al., 2006; Salumäe et al., 2014; Tangorra et al., 2011) and can be used for passive flow control methods, as investigated for vertical-axis turbines such as those presented by Zeiner-Gundersen (2015) or (Hoerner et al., 2019, 2021a). Indeed, the latter studies were originally the motivation for developing the method at hand.

The multi-physical interactions resulting from hyper-flexibility lead to a strong coupling between fluid forces and structural deformations. They are often found, for instance for fluid-induced vibrations or flutter. Numerical methods remain costly and challenging, in particular, if a complex, non-homogeneous structure is subjected to strong deformations (Fabbri, 2022). However, new experimental methods can provide simultaneous measurement of the instantaneous flow fields and structural deformations. This allows for deeper insights into the underlying physical mechanisms as well as investigations of more complex applications of fluid–structure interactions (FSI). Particle image velocimetry (PIV) analysis is the commonly employed method for the investigation of instantaneous flow fields. However, it typically considers a single phase containing the seed particles, so that other structures or phases cannot be tracked directly. Without proper preparation of the experimental setup and data treatment, the computed velocity fields will generally contain spurious vectors inside and in the vicinity of the additional phases and structures, thereby decreasing the reliability of the measurements and constraining the analysis of the whole vector field. To improve quality, it is crucial to mask the non-seeded phases and structures to correctly analyze the seeded phase.

Fujiwara et al. (2004) recognized that there is another advantage in doing so: the obtained masks can be used to reveal the movement of the other phase and its shape (air bubbles in water). Those can be directly used for FSI analysis, allowing for an investigation of the structural displacement or deformation and its relationship to the flow field. Therefore, the automated recognition and masking of non-seeded phases, such as bubbles or structures can improve and enhance experimental studies of multiphase flows and FSI configurations. Since the study of multiphase flows and of the flow around arbitrarily moving bodies or deforming phases (e.g., bubbles) is of much interest for many applications of fluid mechanics, many approaches have been developed to investigate them.

Examples of applications can in particular be found for tracking sand particles within a gas flow (Zhang et al., 2008; Muste et al., 2009; Capone et al., 2015), or for investigating trajectories in a bubble column (Fujiwara et al., 2004; Bröder and Sommerfeld, 2007; Rzehak et al., 2017; Kováts et al., 2017).

To perform a reliable PIV analysis of bubbles and bubble columns, the gas phase or bubbles have to be segmented. A popular method is to use laser-induced fluorescence (LIF) in combination with shadowgraphy (Boëdec and Simoëns, 2001; Lindken and Merzkirch, 2002; Fujiwara et al., 2004; Bröder and Sommerfeld, 2007).

The light scatter at the bubble interface often surpasses the intensity of the light scatter of the seed particles by an order of magnitude or more. This was exploited by several research groups that used digital image processing to derive masks (Cardwell et al., 2011; Gui et al., 1997; Dussol et al., 2016).

Methods relying on brightness intensity and size evaluation are used extensively when investigating particle flows (Muste et al., 2009; Cheng et al., 2010; Diez et al., 2011; Dearing et al., 2013; Capone et al., 2015). This is particularly well-suite when large differences exist between the size of the particles that interact with the flow – very often, sand is used – and the size of the PIV seed particles. In a recent development, purely data-driven methods for particle segmentation have emerged based on an autoencoder, a type of generative adversarial network (Vennemann and Rösgen, 2020). During the encoding step, the tracer particles are lost, while the shape of the sand particle is retained, and can thus be used as a mask. In experiments with free-surface flows, the sudden jump in local light intensity at the interface can be exploited (Sanchis and Jensen, 2011; Jeon and Sung, 2011; Weheliye et al., 2012; Vested et al., 2018).

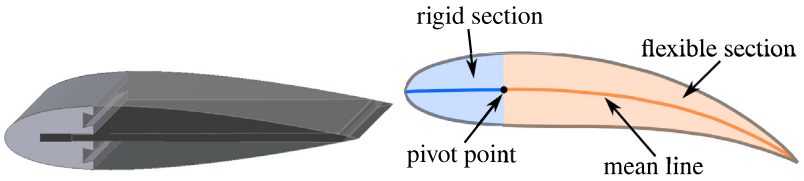

Fig. 1. (Left) Design of the flexible hydrofoil; (Right) Flexible and rigid section of the foil, with the pivot point at their interface and the mean line, here defined as the points midway between the upper and lower surfaces of the foil.

Markers on a body can be tracked with a stereoscopic camera setup, which allows for building a three-dimensional body that is then translated back to the image needed for masking (Tregidgo et al., 2013; Nikoueeyan and Naughton, 2018; Fatiha et al., 2019). The differentiation between tracking points and tracer particles can be achieved by a minimum filter in the time domain if the body moves sufficiently slower compared the tracer particles within the fluid (Mitrotta et al., 2019). Deriving complex shapes from the deformation field of a projected pattern of structured light is also a well-known technique. It has been successfully implemented for surface deformation measurements of a flexible hydrofoil (Hoerner and Bonamy, 2019), which allows for capturing the 3D deformations of the surfaces from 2D single camera recordings. Commercially available laser-line profile scanners have been used to measure the deformation of a flexible sheet along one axis (Ducoin et al., 2012; Kalmbach and Breuer, 2013; Akcabay et al., 2014). The light scatter induced by the PIV light sheet was used for a similar purpose by several researchers (Rojratsirikul et al., 2009; Gomes et al., 2011; Nikoueeyan and Naughton, 2018).

Finally, it should be noted that seed particle displacement does not necessarily have to be recorded by a camera: (Hessenthaler et al., 2017) used magnetic resonance imaging (MRI) to measure the position of seed particles without any need for masking the flexible rubber body present in the study.

It is often possible to generate accurate masks without tracking the second phase, thereby greatly simplifying the experimental setup. However, this translates into a segmentation problem for digital image processing. This issue has already been investigated extensively for gas–liquid phase segmentation (Gui et al., 1997; Cardwell et al., 2011; Sanchis and Jensen, 2011; Jeon and Sung, 2011; Weheliye et al., 2012; Dussol et al., 2016), but to the knowledge of the authors not yet for the segmentation of flexible bodies within a fluid flow acquired with a single-camera setup. Additionally, the suitability and precision of the computed masks for quantifying the deformation of the body have not been quantitatively assessed yet.

In this study, we aim to: (1) determine the body's deformation resulting from the fluid–structure interaction, and, (2) provide an exact masking of a highly flexible body based on the evaluation of the local light intensity. The central objective is to provide a simple and accurate tool to capture the full FSI from a single measurement and to improve the PIV results. The proposed physics-informed method uses apriori knowledge of the flexible structure in particular its bending characteristics, in conjunction with morphological image processing. As an application case, an actively pitched and highly deformable hydrofoil experiment in the water tunnel at LEGI Labs Grenoble is used. The results of the experiment's reference case with known shape serve as an evaluation case of the accuracy of the method itself deploying the PIV raw footage of the known geometry. A test case from synthetic data similar to this example has been created and allows for the quantitative determination of the accuracy of the developed procedure. Although the method is tailored towards this particular data set and may not be an out-of-the-box solution for a different body or a different experimental setup, many steps of the proposed method are universal. Consequently, this publication serves as a description of a general method and provides a computational framework adaptable to the specific needs of any other similar experimental work. This is of particular interest for FSI studies where a low-order structural model already exists which can be exploited to significantly improve the accuracy and reliability of the method.

2. Methodology

The data used in this study is based on an FSI case of a highly flexible hydrofoil for the passive flow control in cross-flow tidal turbines performed in a closed water tunnel in a fully turbulent flow (chord-based Re≈250.000). The hydrofoil with a NACA0018 shape consists of (1) a rigid front section from the leading edge to the pivot point (placed at 0.25C), and (2) a flexible body in chord-wise direction in between the pivot point and the trailing edge, as can be seen in Fig. 1. The rigid tip section was milled from aluminum and can be considered rigid, while the flexible section consisted of a silicone body with a thin, carbon-fiber-enforced composite plate in the middle to provide adequate stiffness. The silicone body provides the external shape. Yet, its contribution to the stiffness is negligible as its Young's modulus is about 10 000 times lower than the modulus of the composite material. All details about the experimental base setup can be found in Hoerner et al. (2019, 2020).

For the PIV setup, a two-dimensional planar PIV high-speed setup (2D2C) with continuous recording at a frame rate of 4000 Hz was chosen, using a Phantom V2511 camera with specifications given in Table 1. Further details concerning the PIV measurements can be found in Hoerner et al. (2021b). The hydrofoil was actively pitched along a specific trajectory

Table 1
Specifications of the PIV setup.

chord-based Reynolds number	250 000
mean flow speed	3.5 m s^{-1}
maximal inclination	30°
image acquisition rate	4 kHz
force & angle acquisition rate	1 kHz
resolution	1280 × 800 pixel (px)
PIV type	high-speed 2D2C, single shot
illumination	continuous laser
flow field capture	instantaneous

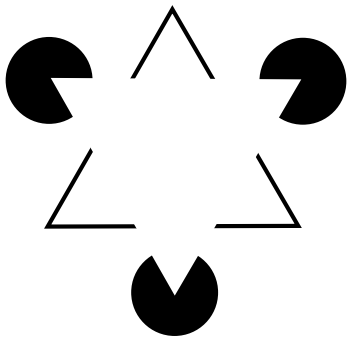

Fig. 2. Kanizsa's triangle: a visual illusion comparable to how the foil is recognized by human perception (Kanizsa, 1955).

representing the variation of the angle of attack for a blade of a Darrieus vertical-axis turbine during each turn of the rotor. The angular position of the drive system performing the pitch motion was recorded by the drive encoder with a frequency of 1000 Hz. The light sheet generated by two opposite continuous lasers had a thickness of 2 mm. The seed particles were hollow glass spheres with a 10 μm diameter.

A detailed description of the process conditions (foil dimension, trajectory, measured signals) is provided in Hoerner et al. (2021a).

While looking for an appropriate algorithm that provided automated mask generation of the deforming structure, it became apparent that established methods that segment visible objects within a picture, e.g. bubbles, are not applicable here. The challenge of the problem stems from the fact that the contour of the foil, which is easily recognizable for a human being, is rather an 'illusory contour' – the visual illusion that evokes the perception of an edge where there is none (von der Heydt et al., 1984). Fig. 2 depicts a well-known example of this.

The task was therefore to recognize this illusory contour in the PIV raw data. Unfortunately, in contrast to the visual perception of human beings, identifying such contours poses a significant challenge to image recognition algorithms. All existing algorithms show specific shortcomings, as described next.

Edge detection as done by Bröder and Sommerfeld (2007) cannot be employed in this study, as there is no visible edge present in the image. Shape-matching of the whole body shape by (cross-)correlation (Gonzalez and Woods, 2008) could perhaps be done using numerous pre-processed bodies at various pitch angles and flexures, but seems impractical due to the sheer amount of cases that would need to be stored and loaded for this purpose. Feature matching would simplify the matching process by breaking the shape into smaller pieces (Jeon and Sung, 2011); however, the size of these pieces needs to be chosen according to the bending gradient of the foil. It is unclear whether these small features could still match at the end the overall foil geometry since, the smaller the representation, the more local seeding density will vary. Some spatial averaging would probably be required at the end, interfering with the procedure. Additionally, the occasional occurrence of outline reflections might lower the recognition ability.

Radon transform has been used with success for wave detection (Sanchis and Jensen, 2011), but is not straightforward to implement when handling closed objects. It would be necessary to either split the upper and lower surface of the foil before recognition or to reliably discern between the two from the results of the Radon transform. Otherwise, it would be unclear whether the recognized section comes from the upper or lower surface of the foil, and a closed body would not be suitably reconstructed.

The local variance of the illumination, as applied by Weheliye et al. (2012), was applied in this study as well; however, the method was not able to distinguish with sufficient accuracy between the body and the fluid.

A somewhat related masking challenge successfully used region-growing to delimit the particle-containing area (Dussol et al., 2016). However, our own results with this approach were disappointing: the seed density was not high enough to reliably return the shape of the foil.

The strongest bias comes from the foil's shape, while another comes from its non-homogeneous composition, with a rigid part at the leading edge (between position 0 and 0.25 on a normalized mean line (C)), and a flexible part between

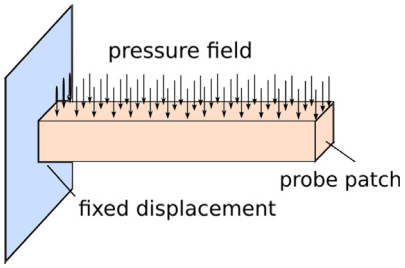

Fig. 3. Clamped beam as mechanical model for the flexure of the foil.

(a) stack and binarize frames (b) assess local illumination (c) fill holes & smoothen outline

(d) estimate neutral axis (e) draw outline

Fig. 4. Processing steps of the implemented algorithm for an exemplary foil position during its movement.

0.25 and 1 C. The pivot point lies at the interface between the two sections (at 0.25 C) and is located on the mean line (synonymously used for camber mean-line or camber line), which is the locus of points midway between the upper and lower surfaces.

The design considered in the study is shown in Fig. 1. Concerning foil thickness, the 4-digit NACA convention (Jacobs et al., 1933) will be used subsequently. It defines the thickness to be the distance between the upper and lower surface along the line normal to the mean line.

3. Procedure

Knowing the flexible and rigid sections of the foil, the neutral axis chord of the profile was modeled under the assumption of a clamped beam with its behavior described using the Euler–Bernoulli beam theory and illustrated in Fig. 3.

Even though the real structure is a plate rather than an Euler–Bernoulli beam, the primary objective of the experiment was to implement a case that allows for a simplified 1D model of the structure within a 2D flow that we measured using 2D2C high-speed PIV. 3D structural effects are generally present in the real system and have been investigated thoroughly in Hoerner and Bonamy (2019). For the method presented here, they have been considered to be negligible here, as we evaluate the hydrofoil only in the light sheet of the PIV system which has a thickness of less than 2 mm. The foil's outline was computed with the respective distance from the neutral axis for each point along the chord. Example images produced by each of the individual steps of the procedure are shown in Fig. 4.

The proposed method performs the subsequent steps to detect and mask the profile cross-section in a series of image processing stages:

Denoise, Stack & Binarize Frames (Fig. 4(a)): Initially, the image is denoised by setting a relative threshold, which regards pixel values above a certain percentile of the distribution of all pixel values within the image as signal and below as noise. Thereafter, consecutive frames are stacked to increase the difference in seed density between the flexible foil and the surrounding fluid. However, this step must be carefully implemented; while it increases recognition accuracy, it simultaneously reduces temporal resolution. Excessive stacking of frames blurs fast movements of the foil, thus diminishing detection accuracy. For subsequent processing with binary kernel operators, the image is binarized where anything above 0 is set to 1. Additionally, the image is cropped with a static window to the area of interest around the foil body to improve performance.

Assess Local Illumination Density (Fig. 4(b)): To assess the seed density within a certain area of the image, a convolution is applied with a matrix that contains ones exclusively arranged in a round shape. This is done by shifting this matrix or kernel successively over the image, multiplying corresponding elements, and summing them to create a new image. The area is regarded as foil body if it is above a threshold, or surrounding fluid if it is below, in our case best results are achieved if this threshold is 1. This method is comparable to the so-called majority filtering proposed by Dussol et al. (2016) and can be found in the reference work regarding digital image processing by Gonzalez and Woods (2008, p. 728). The associated threshold depends on the aggressiveness of the noise removal done in the previous step. In our case, the best strategy was finally found to denoise aggressively and put the threshold at 1 – the whole window will be regarded as fluid if one pixel is active.

Postprocess the Obtained Shape (Fig. 4(c)): Despite the foil body being recognized, holes within that body and islands within the fluid remain. In some parts of the fluid, no seed particles are found, while reflections within the foil body lead to falsely recognized fluid. The resulting artifacts are removed by morphological processing using the open-source toolbox called Scikit-image (van der Walt et al., 2014): The holes in the body are removed by binary closing, a combination of a binary dilation followed by a binary erosion; this also smoothens the shape. The islands in the fluid are removed by evaluating the size of all islands and remove all but the largest, the foil body. Unfortunately, as a result of the smoothing, the narrow leading edge got unintentionally removed as well which will be corrected in the proceeding step.

regions

Retrieve Meanline To compute the meanline, a Laplace filter first obtains the outline of the body. Then, for each index along the chordwise axis, the mean of the upper and the lower value is computed to obtain the meanline. As a result of the preceding binary closing operation, the trailing edge got removed. To restore it, the whole meanline is fitted with a third-degree polynomial fit which is extrapolated towards the trailing edge. This bending model stems from the assumption that the carbon-fiber composite can be considered to behave like a beam, clamped in the aluminum head, and bent by an end-load force. This is a standard case from the Euler–Bernoulli beam theory, in which the deflection curve is an exponential function of the third order. Several assumptions are required for this model: the beam must feature a constant bending stiffness, the elasticity must be linear, the bending must be purely axial, and the diameter must be invariant during flexure. In the case at hand, these premises were found to be met with negligible error (Hoerner et al., 2019). To give the meanline the correct length, it is first measured from the pivot point which serves as a fixed reference and then cut to the length known from the design specification.

Incorporate the Physics (Fig. 4(d)): Since the profile head consists of aluminum no bending occurs in this section. Thus, the mean line at the head is a straight segment with an inclination equal to the instantaneous pitch angle.

As data regarding the pitch angle exists from the drive's position feedback, the mean line between the rigid head and the pivot point is replaced by a straight line at the instantaneous pitch angle. To achieve a smooth transition between the two sections of the meanline, sample points are taken along both segments. All points are then fitted with a single polynomial fit of 4th order to account for the additional points in the rigid section. All points are then fitted with a single polynomial fit of 4th order to account for the additional points in the rigid section. An analysis of the data revealed negligible differences between 4th order and higher order fits, accordingly the lowest fit order was chosen. The amount of sample points is guided by the number of distinct samples needed to inconspicuously describe a linear regressive function. This is equal to the number of parameters that are estimated, as each sample reduces the degree of freedom in the linear system of equations by one. As shown by $\hat{y} = \hat{\beta}_0 + \hat{\beta}_1 x_1 + \hat{\beta}_2 x_2^2 + \cdots$, the amount of parameters is equal to the degree of the fit function plus one. In our case, this leads to 4 sample points for the flexible section and 2 for the rigid section. However, the density of sample points from the rigid section is increased compared to the flexible section, as the confidence in the accuracy of the data is higher; shown in Fig. 5 for the rigid front section of the profile. To locate the interface between the flexible and the rigid sections in the image as well as their respective beginnings and endings, the pivot point served as a reference.

Mitigate Image Recognition Errors: The points obtained from the mean line are filtered using a two-way (to remove an artificial phase shift), second-order low-pass Butterworth filter along the time axis (critical frequency/sample frequency = 0.1). This is done separately for both directions (x and y) in the image along the time axis. This process removes sudden jerks which can be considered as beyond the range of motion or acceleration and as an additional bias for the model. No filter was employed along the mean line itself, as this would violate the model assumptions.

Combine with NACA-Model & Postprocess (Fig. 4(e)): Using the mathematical description of a NACA0018 model, vectors from its mean line to the corresponding outline point were obtained. The number of points in the synthetic mean line was chosen equal to that of the recognized mean line. In consequence, for each point on the recognized mean line, a surface normal was computed and multiplied by the distance between meanline and outline of the undeformed NACA model from that particular chordwise position. The resulting vector was shifted to its respective, actual point along the mean line. In this manner, the NACA shape with the initially linear meanline can be projected onto the deformed mean line, as depicted in Fig. 6 (Left).

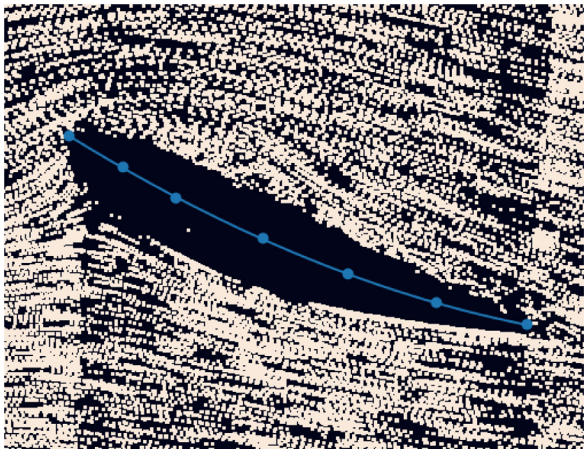

Fig. 5. The computed points along the mean line are shown interpolated by a 3rd-degree polynomial fit in a stacked frame. The seed particles are dilated for better visibility. Concerning the frontal rigid section, a larger number of points has been set to increase its relative effect in the fit.

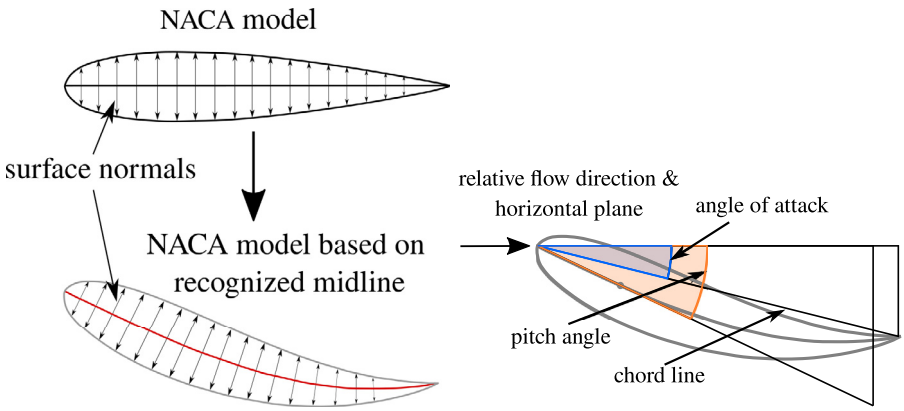

Fig. 6. (Left) Computation of the outline by the use of surface normals obtained from the NACA model; (Right) Angle of attack used in the comparison between measurements. The angle of attack is defined as the angle between the relative flow direction and the chordline. The chordline is defined as the straight line connecting the leading and trailing edges.

The source code has been made public and is available online,[1] licensed under GPLv3. It is written in Python and makes extensive use of the `scipy.ndimage` library (van der Walt et al., 2014), as well as of the Numerical Python (NumPy) package (van der Walt et al., 2011). The processing of 16,500 frames – the entire film length of the setup – with an output of one mean line for each frame, takes less than 20 min using an Intel Xeon CPU E5-2630 v3 at 2.40 GHz on a single thread. Generating and applying the respective mask takes about 5.5 h on the same system. This indicates that the bottleneck for the computation occurs in I/O operations, primarily from loading and saving the masked images to disk through a network drive. While the code is written for parallel execution, the parallelization is not implemented in practice, since performance gains are not to be expected as a consequence of the I/O limitation in the study presented here.

The framework with which the PIV computation was achieved, FluidImage (Augier et al., 2016), natively supports image pre-processing. This would allow for masking of the images without writing them to storage. After computing all mean lines, these lines could be saved and later accessed by FluidImage to create the instantaneous mask. Using this approach, high-performance gains are expected. The implementation of this parallelization feature will be considered as well as an integration of the source code into the FluidImage project in a future study.

4. Results & discussion

To assess the accuracy of the results, the algorithm is employed on synthetic data. This allows for a quantification of the limits of the methodology by implementing a stepwise reduction of the seed density.

[1] https://github.com/ikoesters/FSI_tracking

After the validation, the method is applied to real data of a rigid hydrofoil (with an exactly computable position), and finally on a flexible hydrofoil test case, where a qualitative assessment is performed.

4.1. Method validation with synthetic data

A significant factor in the usefulness of the method is its robustness regarding variations in seed density. Thus, an effort was made to quantify the influence of this parameter. The term summation window is used here for a convolution kernel consisting entirely of ones; effectively summing up all values within the window and storing the result in the window's center. The step size of this window, also called stride, is one pixel. The proposed method was employed on images considering different seed densities; additionally, a second parameter controlling the size of the summation window within the segmentation algorithm was set independently to study whether a larger window could counterbalance lower seed densities. To vary the seed density in a controlled and accurate manner, synthetic data was generated with a visual resemblance to the images for the final test case. A simple generation algorithm was chosen to reduce the underlying variability.

The algorithm first randomly initializes an array, serving as the particle-seeded background of the image. This array is binarized with a high threshold, resulting in a sparse particle seed with an area of 1 px each. Afterward, the array is dilated with a 3×3 px kernel for a realistic seed particle size and brightness variation. Different brightness emerges in cases where seed particles are generated in the direct vicinity and overlap. In the resulting image, these particles get deleted within an area corresponding to the geometry of a four-digit NACA profile (NACA15-5-18) according to Jacobs et al. (1933) to produce an illusory contour at a high inclination angle, somewhat comparable to the real data set (see raw images underneath the boxplot in Fig. 7 for an illustration). This specific shape was chosen as it was manually determined from high-speed recordings of the load-deformed hydrofoils in the study at hand. The inclination angle of this foil is quantified by the angle from the leading to the trailing edge relative to the horizontal plane (as shown in Fig. 6 (Right)), which we will subsequently call the angle of attack. Its real value in the considered problem is 24.2° from the pivot point or 0° from the leading edge to the trailing edge.

Additionally, reflections and other false positives are added with the same method as the generated seed, but with an adjusted threshold. The area of a reflection is 1 px^2 with a value that is sufficient to trigger the algorithm; their number was chosen to visually resemble the real data at hand. This results, on average, in 3 (mean = 2.98, std = 1.84, N = 500) false positives, which amounts to an error rate of 50 ppm in relation to the foil size in pixels. A total of 100 images per seed density with randomly distributed seed particles were computed, without altering the foil shape or position over this period to give consistent and comparable results. The accumulated seed density in the real data can be freely chosen as a first step when employing our method, by controlling the number of stacked images in the process. Here, the seed density was set between $200 - 750$ $\frac{\text{particles}}{(100\times100)\,\text{px}^2}$; the recognition quality below the lower limit is not adequate, while an excessive number of stacked frames would be necessary to exceed the upper limit. For the final example considered in our work, this range represents a stack size between 4 and 10 images, which is realistic. It should be noted that this leads to a time-averaging filter comparable to a rolling average in the deformation measurements, with a window in the stack size. To provide a realistic and conservative measure of the capabilities of the method, we chose a static case that does not employ any low-pass filtering, as cut-off frequency and gain are application-specific parameters. Lower movement speeds could potentially benefit from a reduced cut-off frequency, resulting in improved outcomes. Our decision to employ a static case without any filtering was made to circumvent this issue; this overestimates the error.

Fig. 7 shows the recognition error (y-axis) of the algorithm in relation to different seed densities (x-axis) and the size of the summation window (colored bars). In the application at hand, the effective angle of attack for the deformation assessment is of interest, while for evaluating the masks we use intersection over union (IoU) as a metric, a similarity measure that computes how much two masks intersect relative to the area. It is the method performance measures in object detection commonly based upon (Rezatofighi et al., 2019-06). Additionally, we include the root-mean-square error (RMSE) to allow comparability to other methods.

It can be observed that within selected parameters the algorithm shows good performance over a wide range of seed densities. However, an average error of about 1° was observed in all cases. As can be seen in Fig. 9, the angle of attack and the error on it are positively correlated. Since the foil only briefly reaches high angles of attack in the designated application, this level of error was considered uncritical, and no further effort was spent to investigate the source.

If the algorithm was to be applied, this problem can be circumvented by a correction function as the error was systematic and reproducible. However, to allow comparability this has not been done here.

While the larger window size has an increased chance that seed particles are present similar to a higher aperture of a camera, the greater size reduces the resolution of the segmented image available for the subsequent algorithm steps which diminishes the recognition quality. Additionally, the particles placed inside the structure have a much more pronounced effect. This can be observed at the lowest two seed densities where the medium-sized window balances out both effects and achieves the best error rate. At higher seed densities the benefit of the greater size diminishes and the smallest summation window performs markedly better than the others. The best results are therefore a trade-off between the two opposing effects and have to be determined in the specific case. The outliers within the investigation marked with diamonds, would likely be corrected by the low-pass filter, exploiting the structural similarity within small sections of the time-domain.

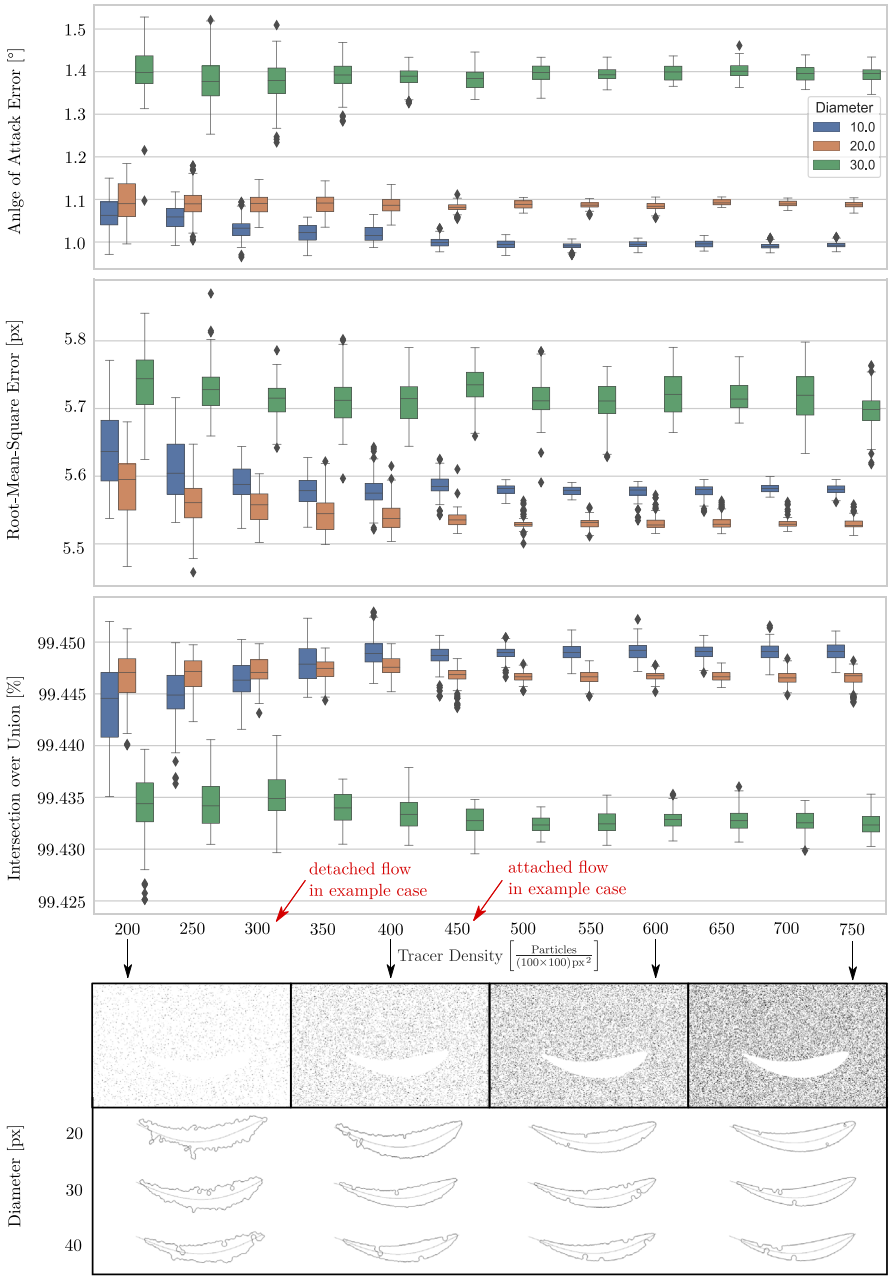

Fig. 7. Detection quality in relation to seed density and summation window diameter. The metrics used in our analysis include the difference in angle of attack, the intersection over union (IoU) for evaluating mask accuracy, and the root-mean-square error (RMSE) of the x–y distance between the true and identified points. Whiskers represent $1.5 \times$ IRQ (interquartile range), sample size is 100 images each. Recognized foils are shown below, selected from different source images to illustrate their respective differences.

In the next step, the impact on the recognition quality of regions with a reduced seed number density due to flow detachment or in a wake was simulated in a dedicated investigation. The image was artificially separated into two regions having distinct seed densities, with an interface roughly located along the camber line. The difference in the seed density was adjusted dynamically, the sparser side containing 66 % of the density on the dense side. This ratio was derived from observations of real data, where a manual count performed on multiple regions and images produced an average seed density of around 75 $\frac{\text{particles}}{(100\times100)\,\text{px}^2}$ in the attached flow, compared to 50 $\frac{\text{particles}}{(100\times100)\,\text{px}^2}$ within the detached flow before stacking the frames to accumulate the seed density.

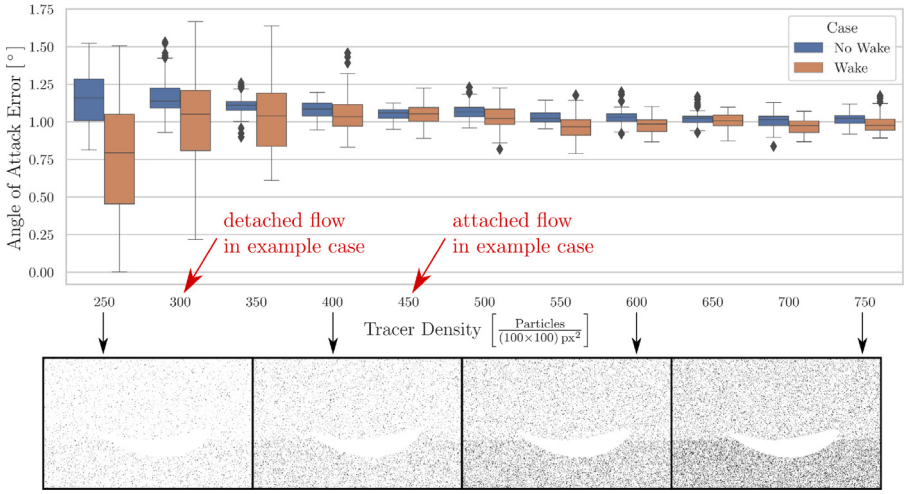

Fig. 8. Detection quality between a simulated region with low seeding density (detachment, wake) compared to the region with normal seeding density (attached flow). The seed density on the horizontal axis is that of the dense region. Whiskers represent 1.5 × IQR, the sample size is 100 images each.

The lower bound of 300 for the seed density in the tests was chosen as this results in a density of $300 \times 66\% = 200 \frac{\text{particles}}{(100\times100)\,\text{px}^2}$ in the detached flow. Higher measurement uncertainty is present in all investigations of the wake case, as can be observed in Fig. 8. Additionally, the bias observed in the last comparison is present as well, best visible in the densely seeded cases which experience low variance. If the value of 1° is assumed to be the correct measurement, the largest deviation of the 1.5×inter-quartile range (IQR) which includes 99.3 % of all values is used as a rough estimate of quality. The largest difference is observed in the case with the lowest seed density where the largest deviation of the wake-case is 1°, while the non-wake-case experiences 0.5° leading to a disparity of 0.5°. Both were evaluated as non-significant for our case. In an exciting recent advancement, another solution to the problem of illusory contour segmentation problem has been proposed (Li et al., 2021); through creating an unstructured mesh in which each tracer particle represents a node. As the seeding density within the other phase is lower, the edges between nodes are longer and are removed through a threshold. Now unconnected nodes are pruned and a smooth curve is subsequently fitted over the division.

4.2. Application on real data

As aforementioned, experiments involving a hyper-flexible NACA0018 hydrofoil subjected to forced oscillation within a closed water tunnel at the LEGI laboratory in Grenoble have been performed (Hoerner et al., 2019; Hoerner and Bonamy, 2019; Hoerner et al., 2020, 2021b,a). The hydrofoil had a chord length of 66 mm, yielding a chord-based Reynolds number of Re = 200,000 when subjected to a flow velocity of $3\,\text{m}\,\text{s}^{-1}$. The forced oscillation was controlled by angle, following a predetermined trajectory that mimicked the flow experienced by a blade in a vertical-axis water turbine. The angle of incidence ranged from −30° to 30°. The entire experiment including set-up, blade models, and the resulting flow fields can be found in Hoerner et al. (2021a). To start with a validation case with known geometry, the algorithm was first employed on the rigid version of the foil. In that case, the mean line can simply be computed from the position feedback of the driver encoder, since no significant deformation occurs.

In Fig. 9 shows the mean measurement error in comparison to the position feedback from the driver encoder, with a mean absolute error of 0.84°. It has an apparent periodicity with the same frequency as the position feedback, however with a phase shift. Tests performed on a limited amount of different motion trajectories and frequencies could not yield a common set of parameters to fit their distinct error function. It was decided against a correction function, as the mechanics behind the error could not be narrowed down. However, the overall magnitude of the error correlates with: a) occurrence of detached flow and (b) occurrence of reflections inside the foil. The sensitivity to detached flow has been studied with the help of synthetic data earlier and is also a challenge for the cross-correlation algorithm of the PIV algorithm. In a test case with static stall conditions, the most unfavorable conditions, the mean absolute error reached 2°. There is by the knowledge of the authors currently no available method to put this method into perspective. Dussol et al. (2016) used a very similar technique, however a validation of the segmentation accuracy was not performed. Hoerner and Bonamy (2019) used structured light to measure the deformation in 3D, while also performing a validation. They report a mean absolute error of 0.66 mm over a profile with a 66 mm chord line, which translates to an angular error of 0.01°. Even though this error is almost an order of magnitude lower, it requires a separate measurement setup while also being mutually exclusive to the PIV measurement due to the necessity of a reflective surface of the body.

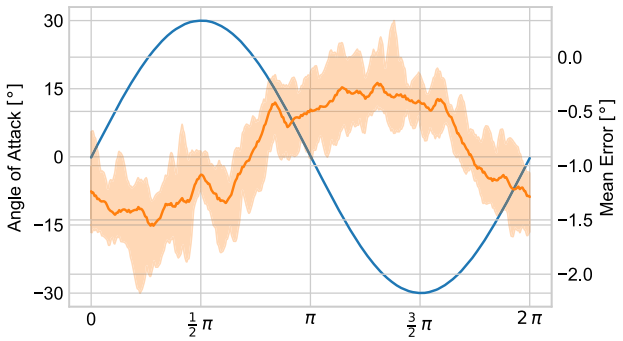

Fig. 9. The orange line shows the mean measurement error (right ordinate) over a full period at 3.1 Hz from a rigid hydrofoil averaged over 12 periods with the faded area representing the minimum and maximum value for each step. The blue line shows the sinusoidal position feedback from the drive system for comparison (left ordinate). (For interpretation of the references to color in this figure legend, the reader is referred to the web version of this article.)

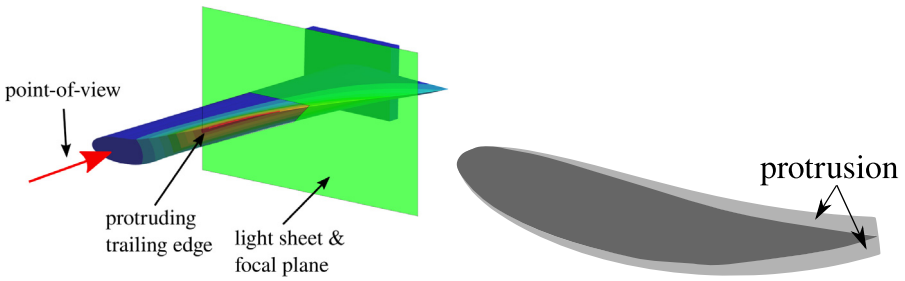

(a) Occlusion Due to Eigenmodes (b) Protrusion of Mask

Fig. 10. Due to the eigenmodes of the structure, the body section closer to the camera's point-of-view occludes part of the deformation along the focal plane. Here, only one single eigenmode is shown for a better visibility. Mask after applying the linearly decreasing protrusion (i.e., artificial thickening).

4.3. Productive use in a flexible foil setup

Expanding on the aforementioned experiment, a highly flexible foil was used to investigate dynamic stall conditions between rigid and flexible foils. The dynamics of the dynamic stall event which occurred at every period of the enforced motion trajectory lead to a stochastic component in the deformation of the foil in the time domain. This made it impossible to independently quantify the accuracy of the method in this case without a second calibrated measurement data source. However, considering the previous investigations on the synthetic data of highly deformed foil and the tracking of a rigid foil on real data which yielded similar results, we can be confident about the adequacy of its performance. This was supported by visual inspection of the masked footage, which showed good tracking but revealed an apparent mismatch between the shape of the trailing edge in the footage and the mask. We determined this to be a result of the span-wise bending modes of the foil, as shown in Fig. 10(a). To account for this effect in the masking procedure, the recovered NACA shape was artificially enlarged by summation of a linearly decreasing term starting from the trailing edge, as shown in Fig. 10(b) for the final mask. Fig. 11 shows the combined PIV and FSI analysis for a flexible hydrofoil. While the diagram in the middle provides the reduced angle of attack due to the passive flow adaptation (blue line) for the instantaneous pitch angle of the blade (orange line). The diagram is embedded in the corresponding flow fields from the 2D2C high-speed PIV for particular points of interest during the oscillation period. The mask and the deflection were calculated with the methods at hand.

5. Conclusions

In this work, we showed that conventional image recognition can be constrained by physical assumptions of the system to greatly improve the recognition quality. The mentioned assumptions include kinematic assumptions on the bending shape, a dynamic assumption regarding the maximum oscillation frequency and morphological knowledge about the soft body. The benefit of the method is twofold: (a) providing a simple way to simultaneously measure the flow field and structural deformation with a single measurement, (b) creating the masks of the soft body undergoing FSI, which is a necessary part of the PIV analysis. The uncertainty of the method was found to be small enough to derive meaningful

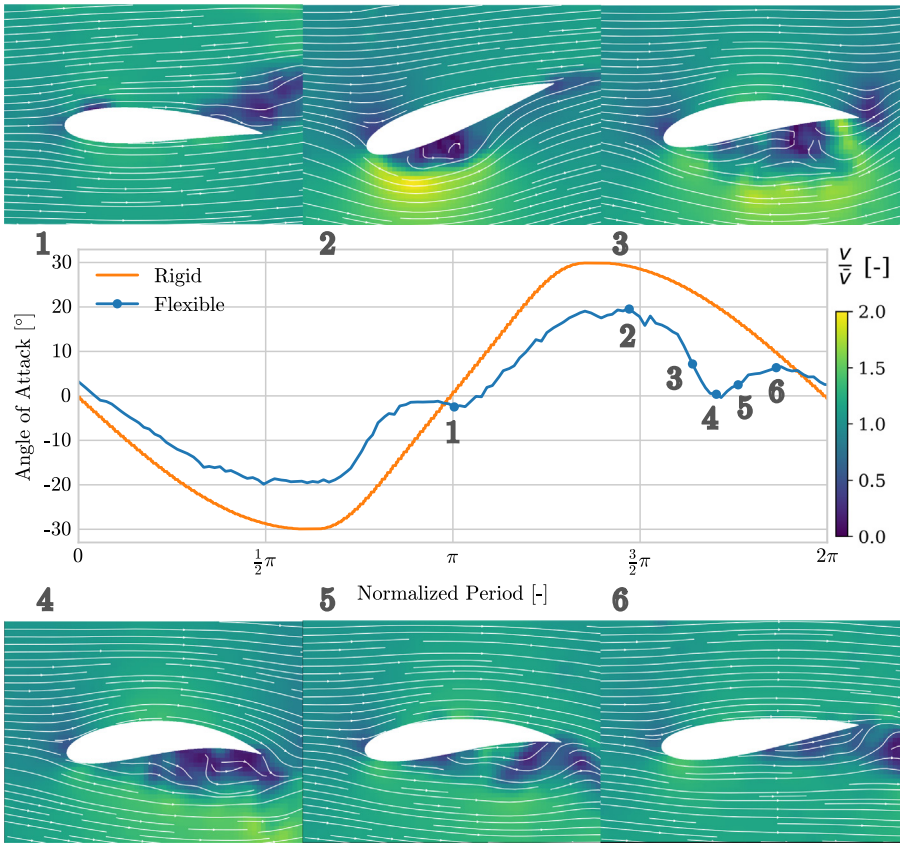

Fig. 11. Combined FSI and PIV analysis from a single image source. A hypothetical rigid blade for comparison to illustrate the degree of deformation.

conclusions for relevant FSI configurations. In a case study with a rigid hydrofoil actively pitched between −30° to 30°, the mean absolute error in the angle of attack was found to be sufficiently low at 0.8°. The presented method has already successfully been used in a recent FSI study to investigate the benefit of passive flow control with the use of a hyper-elastic structure (Hoerner et al., 2021b,a) by exploiting the mentioned benefits. However, certain requirements need to be met to yield satisfactory results: the body itself cannot be reflective or have reflective parts and sufficient particles need to be present for differentiation between body and surrounding in the image recognition step. Additionally, the method necessitates sufficient body thickness, rendering it unsuitable for elastic sheet models. An alternative approach, like the one used by Dussol et al. (2016), which leverages abrupt light intensity variations due to PIV light sheet scattering may be more fitting in this case. The subsequent enhancement of recognition through a kinematic model, as shown here, remains relevant. The sensitivity of the algorithm regarding the latter requirement was investigated through synthetic data controlled for seed density, as well as a wake case discrepancy in the seed density between the hydrofoil sides. Additionally, a naive approach to adapting the image recognition step to low seed densities were investigated by enlarging the kernel size, comparable to pupil dilation in low-light situations.

The method is set up in three distinct steps: (1) kernel-based image recognition, which is high in noise and can fail spectacularly in cases with an ill-arranged combination of reflection within the foil, (2) constrain the bending shape of the chord line to comply with the Euler–Bernoulli beam theory, (3) constrain the dynamic behavior of the deflection with a low-pass filter, (4) surround the obtained chord line with the known shape of the soft body.

As a next step, the method should be validated directly and quantitatively for flexible structures, either using laser interferometry along the trailing edge following (Ducoin et al., 2012), or by laser triangulation as implemented by Kalmbach and Breuer (2013).

Those steps will allow broader use of the method presented here, helping with the analysis of PIV data in fluid–structure experiments and soft actuation or flexible underwater robotics. The proposed method may be uniquely suitable to assess the kinematics of damaged flexible blades. For example, to assess blade motion before, during, and after impact damage with debris or after fatigue. This would allow for a more rapid laboratory assessment method for testing and validating the implementation of self-healing materials and condition monitoring for flexible blades in the future. Linking changes in the dynamic behavior to damage in a soft robotic gripper has recently been shown successfully with a nearly perfect detection and a 97% localization accuracy (Abdulali et al., 2022).

Declaration of competing interest

The authors declare the following financial interests/personal relationships which may be considered as potential competing interests: Wolf Iring Koesters reports financial support was provided by European Commission.

Data availability

A recent snapshot of the Python code along with a small segment of a high-speed video for testing is provided online in the open research data repository hosted by Otto-von-Guericke-University Magdeburg:
10.24352/UB.OVGU-2022-085.
The code is under continuous development. The most recent version can be found on the author's git repository:
https://github.com/ikoesters/FSI_tracking.

Acknowledgments

The authors thank Christian-Toralf Weber and Carsten Laddey (University of Applied Sciences Magdeburg) for providing the foundation for image material from structural mechanics analysis of the hydrofoil. The authors are grateful to Cyrille Bonamy and Pierre Augier (LEGI) for their work and their assistance regarding the incorporation of the PIV framework "FluidImage" into the workflow. Olivier Cleynen is thanked for language editing and commenting on the first manuscript of this article. The authors are grateful to the open science team of the University Magdeburg for their data repository services.

This project is part of the EU Marie Curie International Training Network on Soft, Self-responsive, Smart Materials for Robots (SMART-ITN) and has received funding from the European Union's Horizon 2020 research and innovation program under the Marie Sklodowska-Curie grant agreement No 860108.

References

Abdulali, A., Terryn, S., Vanderborght, B., Iida, F., 2022. Data-driven method for damage localization on soft robotic grippers based on motion dynamics. Front. Robot. AI 9, http://dx.doi.org/10.3389/frobt.2022.1016883.

Akcabay, D.T., Chae, E.J., Young, Y.L., Ducoin, A., Astolfi, J.A., 2014. Cavity induced vibration of flexible hydrofoils. J. Fluids Struct. 49, 463–484. http://dx.doi.org/10.1016/j.jfluidstructs.2014.05.007.

Augier, P., Bonamy, C., Campagne, A., Mohanan, A., 2016. FluidImage, a libre framework for scientific treatments of large sets of images. In: Congrès Francophone de Techniques Laser (CFTL).

Boëdec, T., Simoëns, S., 2001. Instantaneous and simultaneous planar velocity field measurements of two phases for turbulent mixing of high pressure sprays. Exp. Fluids 31 (5), 506–518. http://dx.doi.org/10.1007/s003480100311.

Bozkurttas, M., Dong, H., Mittal, R., Madden, P., Lauder, G., 2006. Hydrodynamic performance of deformable fish fins and flapping foils. In: 44th AIAA Aerospace Sciences Meeting and Exhibit. p. 1392.

Bröder, D., Sommerfeld, M., 2007. Planar shadow image velocimetry for the analysis of the hydrodynamics in bubbly flows. Meas. Sci. Technol. 18 (8), 2513–2528. http://dx.doi.org/10.1088/0957-0233/18/8/028.

Capone, A., Romano, G.P., Soldati, A., 2015. Experimental investigation on interactions among fluid and rod-like particles in a turbulent pipe jet by means of particle image velocimetry. Exp. Fluids 56 (1), 1. http://dx.doi.org/10.1007/s00348-014-1876-4.

Cardwell, N.D., Vlachos, P.P., Thole, K.A., 2011. A multi-parametric particle-pairing algorithm for particle tracking in single and multiphase flows. Meas. Sci. Technol. 22 (10), 105406. http://dx.doi.org/10.1088/0957-0233/22/10/105406.

Cheng, Y., Pothos, S., Diez, F.J., 2010. Phase discrimination method for simultaneous two-phase separation in time-resolved stereo PIV measurements. Exp. Fluids 49 (6), 1375–1391. http://dx.doi.org/10.1007/s00348-010-0878-0.

Dearing, S.S., Campolo, M., Capone, A., Soldati, A., 2013. Phase discrimination and object fitting to measure fibers distribution and orientation in turbulent pipe flows. Exp. Fluids 54 (1), 1419. http://dx.doi.org/10.1007/s00348-012-1419-9.

Diez, F.J., Torregrosa, M.M., Pothos, S., 2011. A comparison between round turbulent jets and particle-laden jets in crossflow by using time-resolved stereoscopic particle image velocimetry. J. Fluids Eng. 133 (9), 091301. http://dx.doi.org/10.1115/1.4004815.

Ducoin, A., Astolfi, J.A., Sigrist, J.-F., 2012. An experimental analysis of fluid structure interaction on a flexible hydrofoil in various flow regimes including cavitating flow. Eur. J. Mech. B Fluids 36, 63–74. http://dx.doi.org/10.1016/j.euromechflu.2012.03.009.

Dussol, D., Druault, P., Mallat, B., Delacroix, S., Germain, G., 2016. Automatic dynamic mask extraction for PIV images containing an unsteady interface, bubbles, and a moving structure. Comptes Rendus Mécanique 344 (7), 464–478. http://dx.doi.org/10.1016/j.crme.2016.03.005.

Fabbri, T., 2022. Development of a high fidelity fluid-structure interaction solver : towards flexible foils simulation (Ph.D. thesis).

Fatiha, M.A., Augier, B., Deniset, F., Casari, P., Astolfi, J.A., 2019. Morphing hydrofoil model driven by compliant composite structure and internal pressure. J. Mar. Sci. Eng. 7 (12), http://dx.doi.org/10.3390/jmse7120423.

Fujiwara, A., Danmoto, Y., Hishida, K., Maeda, M., 2004. Bubble deformation and flow structure measured by double shadow images and PIV/LIF. Exper. fluids 36 (1), 157–165. http://dx.doi.org/10.1007/s00348-003-0691-0.

Gomes, J.P., Yigit, S., Lienhart, H., Schäfer, M., 2011. Experimental and numerical study on a Laminar fluid–structure interaction reference test case. J. Fluids Struct. 27 (1), 43–61. http://dx.doi.org/10.1016/j.jfluidstructs.2010.09.004.

Gonzalez, R.C., Woods, R.E., 2008. Digital Image Processing, third ed., internat. ed In: Pearson Education, Pearson Education Internat, Upper Saddle River, NJ.

Gui, L., Lindken, R., Merzkirch, W., 1997. Phase-separated PIV measurements of the flow around systems of bubbles rising in water. In: ASME FEDSM, Vol. 97. Citeseer, pp. 22–26.

Hessenthaler, A., Gaddum, N.R., Holub, O., Sinkus, R., Röhrle, O., Nordsletten, D., 2017. Experiment for validation of fluid-structure interaction models and algorithms: Experiment for validation of fluid-structure interaction models and algorithms. Int. J. Numer. Methods Biomed. Eng. 33 (9), e2848. http://dx.doi.org/10.1002/cnm.2848.

Hoerner, S., Abbaszadeh, S., Cleynen, O., Bonamy, C., Maître, T., Thévenin, D., 2021a. Passive flow control mechanisms with bioinspired flexible blades in cross-flow tidal turbines. Exp. Fluids 62 (5), 104. http://dx.doi.org/10.1007/s00348-021-03186-8.

Hoerner, S., Abbaszadeh, S., Maître, T., Cleynen, O., Thévenin, D., 2019. Characteristics of the fluid– structure interaction within darrieus water turbines with highly flexible blades. J. Fluids Struct. 88, 13–30. http://dx.doi.org/10.1016/j.jfluidstructs.2019.04.011.
Hoerner, S., Bonamy, C., 2019. Structured-light-based surface measuring for application in fluid–structure interaction. Exp. Fluids 60 (11), 168. http://dx.doi.org/10.1007/s00348-019-2821-3.
Hoerner, S., Bonamy, C., Cleynen, O., Maître, T., Thévenin, D., 2020. Darrieus vertical-axis water turbines: Deformation and force measurements on bioinspired highly flexible blade profiles. Exp. Fluids 61 (6), 141. http://dx.doi.org/10.1007/s00348-020-02970-2.
Hoerner, S., Kösters, I., Vignal, L., Cleynen, O., Abbaszadeh, S., Maître, T., Thévenin, D., 2021b. Cross-flow tidal turbines with highly flexible blades–experimental flow field investigations at strong fluid–structure interactions. Energies 14 (4), 797. http://dx.doi.org/10.3390/en14040797.
Jacobs, E.N., Ward, K.E., Pinkerton, R.M., 1933. The Characteristics of 78 related airfoil section from tests in the Variable-Density Wind Tunnel, no. 460. US Government Printing Office.
Jeon, Y., Sung, H., 2011. PIV measurement of flow around an arbitrarily moving body. Exp. Fluids 50 (4), 787–798. http://dx.doi.org/10.1007/s00348-010-0855-7.
Kalmbach, A., Breuer, M., 2013. Experimental PIV/V3V measurements of vortex-induced fluid–structure interaction in turbulent flow–a new benchmark FSI-pfs-2a. J. Fluids Struct. 42, 369–387. http://dx.doi.org/10.1016/j.jfluidstructs.2013.07.004.
Kanizsa, G., 1955. Margini quasi-percettivi in campi con stimolazione omogenea.
Kováts, P., Thévenin, D., Zähringer, K., 2017. Investigation of mass transfer and hydrodynamics in a model bubble column. Chem. Eng. Technol. 40 (8), 1434–1444. http://dx.doi.org/10.1002/ceat.201600679.
Li, Y., Blois, G., Kazemifar, F., Christensen, K.T., 2021. A particle-based image segmentation method for phase separation and interface detection in PIV images of immiscible multiphase flow. Meas. Sci. Technol. 32 (9), 095208. http://dx.doi.org/10.1088/1361-6501/abf0dc.
Lindken, R., Merzkirch, W., 2002. A novel PIV technique for measurements in multiphase flows and its application to two-phase bubbly flows. Exp. Fluids 33 (6), 814–825. http://dx.doi.org/10.1007/s00348-002-0500-1.
Mitrotta, F.M.A., Sciacchitano, A., Sodja, J., De Breuker, R., van Oudheusden, B.W., 2019. Experimental investigation of the fluid-structure interaction between a flexible plate and a periodic gust by means of robotic volumetric PIV. In: 13th International Symposium on Particle Image Velocimetry. Universität der Bundeswehr München Neubiberg, Germany, pp. 645–656.
Muste, M., Yu, K., Fujita, I., Ettema, R., 2009. Two-phase flow insights into open-channel flows with suspended particles of different densities. Environ. Fluid Mech. 9 (2), 161–186. http://dx.doi.org/10.1007/s10652-008-9102-7.
Nikoueeyan, P., Naughton, J.W., 2018. A photogrammetric approach for masking particle image velocimetry images around moving bodies. Meas. Sci. Technol. 29 (10), 105203. http://dx.doi.org/10.1088/1361-6501/aad9c8.
Rezatofighi, H., Tsoi, N., Gwak, J., Sadeghian, A., Reid, I., Savarese, S., 2019-06. Generalized intersection over union: A metric and a loss for bounding box regression. In: 2019 IEEE/CVF Conference on Computer Vision and Pattern Recognition. CVPR, IEEE, pp. 658–666. http://dx.doi.org/10.1109/CVPR.2019.00075.
Rojratsirikul, P., Wang, Z., Gursul, I., 2009. Unsteady fluid–structure interactions of membrane airfoils at low Reynolds numbers. Exp. Fluids 46 (5), 859–872. http://dx.doi.org/10.1007/s00348-009-0623-8.
Rzehak, R., Krauß, M., Kováts, P., Zähringer, K., 2017. Fluid dynamics in a bubble column: new experiments and simulations. Int. J. Multiph. Flow. 89, 299–312. http://dx.doi.org/10.1016/j.ijmultiphaseflow.2016.09.024.
Salumäe, T., Raag, R., Rebane, J., Ernits, A., Toming, G., Ratas, M., Kruusmaa, M., 2014. Design principle of a biomimetic underwater robot u-cat. In: 2014 Oceans-St. John's. IEEE, pp. 1–5.
Sanchis, A., Jensen, A., 2011. Dynamic masking of PIV images using the radon transform in free surface flows. Exp. Fluids 51 (4), 871–880. http://dx.doi.org/10.1007/s00348-011-1101-7.
Tangorra, J., Phelan, C., Esposito, C., Lauder, G., 2011. Use of biorobotic models of highly deformable fins for studying the mechanics and control of fin forces in fishes. Integr. Comp. Biol. 51 (1), 176–189. http://dx.doi.org/10.1093/icb/icr036.
Tregidgo, L., Wang, Z., Gursul, I., 2013. Unsteady fluid–structure interactions of a pitching membrane wing. Aerosp. Sci. Technol. 28 (1), 79–90. http://dx.doi.org/10.1016/j.ast.2012.10.006.
van der Walt, S., Colbert, S.C., Varoquaux, G., 2011. The numpy array: A structure for efficient numerical computation. Comput. Sci. Eng. 13 (2), 22–30. http://dx.doi.org/10.1109/MCSE.2011.37.
van der Walt, S., Schönberger, J., Nunez-Iglesias, J., Boulogne, F., Warner, J.D., Yager, N., Gouillart, E., Yu, T., 2014. Scikit-image: Image processing in python. PeerJ 2, e453. http://dx.doi.org/10.7717/peerj.453.
Vennemann, B., Rösgen, T., 2020. A dynamic masking technique for particle image velocimetry using convolutional autoencoders. Exp. Fluids 61 (7), 168. http://dx.doi.org/10.1007/s00348-020-02984-w, URL https://link.springer.com/10.1007/s00348-020-02984-w.
Vested, M.H., Ergin, F.G., Carstensen, S., Christensen, E.D., 2018. High-resolution planar two-component PTV measurements in a breaking wave. In: 19th International Symposium on the Application of Laser and Imaging Techniques to Fluid Mechanics. Springer-Verlag.
von der Heydt, R., Peterhans, E., Baumgartner, G., 1984. Illusory contours and cortical neuron responses. Science 224 (4654), 1260–1262. http://dx.doi.org/10.1126/science.6539501.
Weheliye, W., Yianneskis, M., Ducci, A., 2012. PIV measurements in a shaken cylindrical bioreactor. In: 16th International Symposium on Applications of Laser Techniques to Fluid Mechanics. Lisbon, Portugal.
Zeiner-Gundersen, D., 2015. A novel flexible foil vertical axis turbine for river, ocean, and tidal applications. Appl. Energy 151, 60–66. http://dx.doi.org/10.1016/j.apenergy.2015.04.005.
Zhang, W., Wang, Y., Lee, S., 2008. Simultaneous PIV and PTV measurements of wind and sand particle velocities. Exp. Fluids 45 (2), 241–256. http://dx.doi.org/10.1007/s00348-008-0474-8.